



Microscopic model of spin flip-flop processes in crystals doped by rare-earth ions

Hafsa Syed, Adam Kinos , Chunyan Shi,^{*} Lars Rippe, and Stefan Kröll
Department of Physics, Lund University, P.O. Box 118, SE-22100 Lund, Sweden

 (Received 6 May 2022; revised 30 September 2022; accepted 15 November 2022; published 28 November 2022)

Flip-flop processes due to magnetic dipole-dipole interaction between neighboring ions in crystals doped by rare-earth ions are one of the mechanisms of relaxation between hyperfine levels. Modeling of this mechanism has so far been macroscopic, characterized by an average rate describing the relaxation of all ions. Here, however, we present a microscopic model of flip-flop interactions between individual nuclear spins of dopant ions. Every ion is situated in a unique local environment in the crystal, where each ion has different distances and a unique orientation relative to its nearest neighbors, as determined by the lattice structure. Thus each ion has a unique flip-flop rate and the collective relaxation dynamics of all ions in a bulk crystal is a sum of many exponential decays, giving rise to a distribution of rates rather than a single average decay rate. We employ this model to calculate flip-flop rates in $\text{Pr}^{3+}:\text{Y}_2\text{SiO}_5$ and show experimental measurements of population decay of the ground state hyperfine levels at ~ 2 K. We also present a method to measure rates of individual transitions from hole burning spectra that requires significantly fewer fitting parameters in theoretical rate equations compared to earlier work. Furthermore, we measure the effect of external magnetic field on the flip-flop rates and observe that the rates slow down by two orders of magnitude in a field of 5–10 mT.

DOI: [10.1103/PhysRevB.106.184109](https://doi.org/10.1103/PhysRevB.106.184109)

I. INTRODUCTION

Crystals doped by rare-earth ions have hyperfine transitions with unique properties such as long lifetimes and coherence times, for example up to 20 days [1,2] and six hours, respectively, in $\text{Eu}^{3+}:\text{Y}_2\text{SiO}_5$ [3]. These transitions are easily accessible via optical transitions that are inhomogeneously broadened (up to 100's of GHz) and also possess narrow homogeneous linewidths (\leq kHz), enabling their use in quantum memories [4–6] and quantum computing [7–11]. Long-lived, optically deep, and spectrally narrow holes can be burnt in these materials and they can be used in laser stabilization [12–15] and as efficient spectral filters in a medical imaging technique called ultrasound optical tomography [16–20].

Even though hyperfine lifetimes can be as long as seconds or much more, relaxation can be a problem in many of the above applications. It can result in decreased absorption depth when preparing absorption structures, leading to lower efficiency of echoes in quantum memories [[21], Chap. 5.4.3] and degrading of spectral filters [[22], Chap. 5], and the relaxation can introduce background noise when studying gate operations for quantum computing [23]. In general, hyperfine relaxation can occur either via lattice vibrations mediated by phonons (spin-lattice relaxation) or via interactions with

neighboring spins (spin-spin relaxation). Spin-lattice relaxation processes are well understood [24,25] and the mechanism relevant at cryogenic temperatures is the direct process, whose rate increases proportional to the temperature ($\propto T$) and square of magnetic field ($\propto B^2$) [26]. However, various experiments at cryogenic temperatures have demonstrated a decrease in relaxation rates with the application of a magnetic field [27–30]. Furthermore, for the low temperature (~ 2 K) and low fields (5–10 mT) used in this study, the direct process results in negligible relaxation rates. Therefore, the dominant mechanisms responsible for relaxation in these cases are not phonon related but magnetic dipole interactions between dopants. They are known as flip-flop interactions whereby two nearby ions exchange their spins via magnetic dipole-dipole interaction and the interaction strength wanes with distance r as r^{-6} . Studies in Kramers ions like Er^{3+} and Nd^{3+} have used a macroscopic model to explain spectral hole decay due to the flip-flop process by taking a single average rate to be related to the dopant concentration [30] and an average ion-ion distance for the ions in the crystal [29], resulting in a rate $R \propto \frac{n^2}{\langle r \rangle^6}$. However, it has also been reported that this mechanism can lead to nonexponential decays [31–34] and the focus of this work is to develop a model that captures this effect.

Each dopant ion in the crystal is randomly placed in the crystalline structure such that it experiences a different magnetic environment and has different distances to and orientations of its nearest neighboring dopants. Therefore, each ion relaxes with a unique rate and when the relaxation dynamics is studied in a bulk crystal, we see a sum of many exponential decays. In this work, we use a numerical simulation of a host crystal to create a distribution of ion-ion distances. The flip-flop rate between all the pairs of ions is then calculated using Fermi's golden rule. The shape of this distribution of flip-flop rates mimics that of r^{-6} , where r is

^{*}Present address: Zurich Instruments, Technoparkstrasse 1, Zurich, Switzerland.

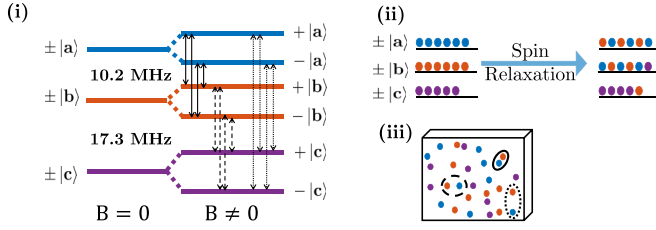


FIG. 1. Representation of spin relaxation via flip-flop interactions in $\text{Pr}^{3+}:\text{Y}_2\text{SiO}_5$, whereby two neighboring ions interchange their state. (i) Ground state hyperfine levels $\pm|a\rangle$, $\pm|b\rangle$, and $\pm|c\rangle$ lose their degeneracy in the presence of an external magnetic field B , forming six levels. The pathways considered for spin relaxation in our simulations are shown with double-sided arrows. (ii) Ions occupying $\pm|a\rangle$ and $\pm|b\rangle$ flip-flop strongly with each other, while those in $\pm|c\rangle$ share weak interaction with either of the other hyperfine levels. (iii) The interaction strength varies with distance r as r^{-6} so closely lying neighbors in the crystal can rapidly flip-flop (shown as solid ovals), while ions separated by larger distances share weaker interaction (shown as dashed and dotted ovals).

the ion-ion distance. We compare the model to experimental measurements of population decay of hyperfine levels in $\text{Pr}^{3+}:\text{Y}_2\text{SiO}_5$. The experiments are done using an alternative method to measure rates of individual transitions using hole-burning spectra. An earlier work [35] used hole-burning spectra in $\text{Pr}^{3+}:\text{YAlO}_3$ to fit 21 parameters to theoretical rate equations. We reduce the number of fitting parameters to 3 by initializing the ground state population in one of the hyperfine levels in a narrow spectral region. Three additional parameters are used to describe the effect of small magnetic fields between 5 and 10 mT on the flip-flop rates on each of the transitions.

The paper is structured as follows. We first introduce the relaxation pathways for flip-flop interactions considered and enumerate the steps in simulating a distribution of flip-flop rates in Sec. II. We then explain the experimental method used to measure population decay in $\text{Pr}^{3+}:\text{Y}_2\text{SiO}_5$ in Sec. III. In Sec. IV, we compare the experiments with simulations to extract the flip-flop rates and also show that the distribution of rates arises from a distribution of ion-ion distance. Lastly, we conclude with some comments on further additions to the microscopic model.

II. MICROSCOPIC MODEL FOR FLIP-FLOP INTERACTION

In this section, we first explain the relaxation pathways and different strengths of each pathway considered in the model with the example of $\text{Pr}^{3+}:\text{Y}_2\text{SiO}_5$. We set up the magnetic dipole-dipole interaction Hamiltonian for a pair of ions and explain the use of Fermi's rule to calculate the flip-flop rate between them. Then, we enumerate the steps in simulating flip-flop interactions and specify the parameters used for $\text{Pr}^{3+}:\text{Y}_2\text{SiO}_5$.

Figure 1(i) shows the three hyperfine levels in the electronic ground state 3H_4 $\text{Pr}^{3+}:\text{Y}_2\text{SiO}_5$ and the twelve relaxation pathways considered in the simulations. Each hyperfine level is doubly degenerate but the degeneracy is lost in the presence of an external magnetic field, giving rise to six levels in total.

It should be noted that conventional labels for the hyperfine levels are $\pm|\frac{1}{2}g\rangle$, $\pm|\frac{3}{2}g\rangle$, and $\pm|\frac{5}{2}g\rangle$, but each level is in reality an admixture of all six hyperfine wave functions. So we instead use the labels $\pm|a\rangle$, $\pm|b\rangle$, and $\pm|c\rangle$. For six levels, we could expect fifteen unique flip-flop transitions. But we do not consider the transitions where only the parity changes, for example transitions of the type $+|a\rangle \leftrightarrow -|a\rangle$, since we do not measure these individually in our experiments. Hence we have twelve pathways in total. In the experiments described in Sec. III, it is seen that the strongest interaction is between ions occupying $\pm|a\rangle$ and $\pm|b\rangle$ (indicated by solid double-sided arrows), while $\pm|c\rangle$ couples weakly to the other two levels (indicated by dashed and dotted double-sided arrows). Figure 1(ii) shows the dependence of strength of flip-flop interaction on the hyperfine level occupied by ions. For example, ions initialized in $\pm|a\rangle$ and $\pm|b\rangle$ flip-flop strongly to give fairly mixed populations (blue and red circles), while ions in $\pm|c\rangle$ (purple circles) flip-flop with either of the other two levels with less likelihood. Figure 1(iii) visualizes how the interaction strength scales with distance as r^{-6} ; thus closely lying neighbors in a crystal interact strongly (shown as solid ovals), while ions far away from each other show weaker interaction (shown as dashed and dotted ovals).

The rate for ion “ i ” to flip from $|x\rangle$ to $|y\rangle$ due to interactions with its “ j ” neighbors initially in the state $|y\rangle$ is calculated using Fermi's golden rule:

$$R_{|x\rangle\rightarrow|y\rangle}^i = \frac{2\pi}{\hbar} \sum_j | \langle y^i \otimes x^j | H_{dd}^{ij} | x^i \otimes y^j \rangle |^2 f(E). \quad (1)$$

It is worth noting that calculation of the matrix elements $|\langle y^i \otimes x^j | H_{dd}^{ij} | x^i \otimes y^j \rangle|$ for all pair of ions makes our model “microscopic,” setting it apart from previous similar works, where this was taken as an average value and related to the concentration of dopants in Refs. [29,30].

Wave functions of hyperfine levels $|x^i\rangle$ and $|y^j\rangle$ are the eigenstates of the spin Hamiltonian and they depend on the external magnetic field \mathbf{B} . They are calculated using the following equation for the spin Hamiltonian, as used in Ref. [36]:

$$H_{\text{spin}} = \mathbf{B} \cdot \mathbf{M} \cdot \tilde{\mathbf{I}} + \tilde{\mathbf{I}} \cdot \mathbf{Q} \cdot \tilde{\mathbf{I}}. \quad (2)$$

The crystallographic axes of the crystal $[D_1 \ D_2 \ b]$ form the common frame of reference for the above calculations. $\tilde{\mathbf{I}}$ is the vector of nuclear spin operators $\tilde{I}_x, \tilde{I}_y, \tilde{I}_z$ and \mathbf{B} is the magnetic field vector. \mathbf{M} is the effective Zeeman tensor and \mathbf{Q} is the effective quadrupole tensor, defined as follows:

$$\mathbf{M} = \mathbf{R}_M \begin{bmatrix} g_x & 0 & 0 \\ 0 & g_y & 0 \\ 0 & 0 & g_z \end{bmatrix} \mathbf{R}_M^T = \begin{bmatrix} g_{xx} & g_{xy} & g_{xz} \\ g_{yx} & g_{yy} & g_{yz} \\ g_{zx} & g_{zy} & g_{zz} \end{bmatrix}, \quad (3)$$

$$\mathbf{Q} = \mathbf{R}_Q \begin{bmatrix} E - \frac{1}{3}D & 0 & 0 \\ 0 & -E - \frac{1}{3}D & 0 \\ 0 & 0 & \frac{2}{3}D \end{bmatrix} \mathbf{R}_Q^T. \quad (4)$$

Each of the above matrices is transformed into the frame $[D_1 \ D_2 \ b]$ using rotation matrices with appropriate Euler angles: $\mathbf{R}_k = R(\alpha, \beta, \gamma)$. The two terms on the right-hand side of Eq. (2) are evaluated according to Ref. [25]: $\mathbf{B} \cdot \mathbf{M} \cdot \tilde{\mathbf{I}} = g_{pq} B_p \tilde{I}_q$ and $\tilde{\mathbf{I}} \cdot \mathbf{Q} \cdot \tilde{\mathbf{I}} = Q_{pq} \tilde{I}_p \tilde{I}_q$,

where $p, q = x, y, z$ and the usual summation rules are to be observed whenever a suffix occurs twice.

H_{dd}^{ij} is the Hamiltonian for magnetic dipole–dipole interaction between an ion i and a neighboring ion j [25],

$$H_{dd}^{ij} = \frac{\mu_0 \hbar^2}{4\pi} \tilde{r}_p^i \tilde{r}_q^j \left\{ g_{ps}^i g_{qs}^j - \frac{3\mathbf{r}_s^i \mathbf{r}_t^j}{|\mathbf{r}^{ij}|^2} g_{ps}^i g_{qt}^j \right\} \frac{1}{|\mathbf{r}^{ij}|^3}, \quad (5)$$

where each of the suffixes p, q, s, t take the values x, y, z . \mathbf{r}^{ij} is the vector connecting the two ions.

It should be noted that using Fermi's golden rule is an approximation that relies on perturbation theory, i.e., the interaction should be weak. In our case the dipole-dipole interaction Hamiltonian H_{dd} is in the order of 1 Hz–1 kHz, and the smallest term in the spin Hamiltonian H_{spin} given by Eq. (2) is in the order of tens of kHz. Thus H_{dd} can be treated as perturbation to H_{spin} .

The last factor in Fermi's golden rule in Eq. (1) is $f(E)$, the density of initial and final states for transitions between two levels in the continuum of initial and final states $|x^i\rangle \otimes |y^j\rangle$ and $|y^i\rangle \otimes |x^j\rangle$, respectively. The form of density of states we use is $f(E) = \frac{1}{\pi \hbar} \frac{\Gamma_{\text{hom}}(\mathbf{B})}{\Gamma_{\text{hom}}^2(\mathbf{B}) + [\kappa_{xy}(\mathbf{B}) \Gamma_{xy}]^2}$, where Γ_{hom} and Γ_{xy} are the homogeneous and inhomogeneous linewidths of the transition $|x\rangle \leftrightarrow |y\rangle$. Γ_{hom} is a function of external magnetic field \mathbf{B} and $\kappa_{xy}(\mathbf{B})$ is a phenomenological addition to describe the increase in inhomogeneous linewidths in the presence of a magnetic field. The details of the derivation of density of states is given in Appendix A 1 and similar expressions have been used to describe transitions between broadened states in different quantum wells, as described in Sec. 3.3 of Ref. [37]. In principle, all pairs of ions are spectrally separated by a different value in the distribution of spin inhomogeneous broadening Γ_{xy} . However, here we focus on the microscopic effect of distances between the ions being different and take an average value for Γ_{xy} .

In brief, the simulation steps required for calculating flip-flop rates are as follows.

(1) A small sphere of a host crystal is simulated, where ions are placed according to the crystal lattice structure [38]. It is doped with a rare-earth ion with the specified concentration. Alternatively, one could also assume a continuous random distribution function of ions to determine the position of nearest N th neighbor, as done in Ref. [39]. More details about modeling the host crystal can be found in [40]. An ion i is picked in the sphere and nearest neighbors j are found. Nuclear wave functions $|a^i\rangle \dots |c^i\rangle$ and $|a^j\rangle \dots |c^j\rangle$ are calculated to be eigenstates of the spin Hamiltonian in Eq. (2) and depend on the orientation of the ion in the crystal and the magnetic field.

(2) The dipole-dipole interaction Hamiltonian for ion i due to interaction with neighbors j is calculated according to Eq. (5).

(3) Flip-flop rates for the transitions between all hyperfine levels are calculated using Fermi's rule in Eq. (1).

In $\text{Pr}^{3+}:\text{Y}_2\text{SiO}_5$, only the ions in site 1 corresponding to the ${}^3H_4 \rightarrow {}^1D_2$ transition at 606 nm were used. The radius of sphere used was 100 nm and the flip-flop rate of ion i was calculated due to the interaction with its 20 nearest neighbors. Pr^{3+} has a nuclear spin $\frac{5}{2}$; thus $\tilde{\mathbf{I}}$ is a (3×1) vector where each element is a (6×6) matrix. The eight basic molecules in a unit

cell of Y_2SiO_5 have four different directions so for any ion i , the tensors \mathbf{M} and \mathbf{Q} in Eq. (2) have one of the four orientations. Values for all the parameters in Eqs. (3) and (4) were taken from Raman heterodyne spectroscopy measurements done in Ref. [36]. The magnetic field was directed along the crystal axis b . Homogeneous linewidths $\Gamma_{\text{hom}}(\mathbf{B}) = \frac{1}{\pi T_2}$ were taken from Refs. [41,42], where the spin coherence time T_2 was measured to be 0.5 ms with zero magnetic field (also measured in Ref. [43]) and 6 ms in the presence of magnetic field of 2 mT. It does not change appreciably even up to 100 mT [41,42], so 6 ms was used for the data with a field between 5 and 10 mT. The values for all the individual transitions have not been measured, so the same was used for all. Furthermore, our experiments do not distinguish between the rates of the form of $|a\rangle \rightarrow |b\rangle$ from $|a\rangle \rightarrow -|b\rangle$, $-|a\rangle \rightarrow |b\rangle$, or $-|a\rangle \rightarrow -|b\rangle$, so we in the following sections sum and average the rates such that only three effective rates R_{ab} , R_{bc} , and R_{ac} were obtained for each ion i . The details of reducing twelve rates down to three are described in Appendix A 2. After this reduction, the model contains six unknowns: the three inhomogeneous spin linewidths Γ_{ab} , Γ_{bc} , Γ_{ac} and the factors describing their magnetic field dependence κ_{ab} , κ_{bc} , κ_{ac} used in the density of states $f(E)$.

III. EXPERIMENTS

Relaxation between spin levels has been studied in many different ways, for example, using methods that combine optical spectral hole burning and RF fields resonant with a hyperfine transition [44–46]. A method to extract rate constants for individual transitions using only hole burning spectra has been used in Ref. [35] but it requires many fitting parameters for each rate equation to be able to keep track of the initial population of any ion that was excited during the hole burning. For example, $\text{Pr}^{3+}:\text{YAIO}_3$ has three hyperfine levels in the ground and excited states. Thus a laser at a single frequency on the ${}^3H_4 \rightarrow {}^1D_2$ transition can excite nine different transitions or classes of ions. So the method in Ref. [35] required 21 independent fitting parameters (18 initial spin populations and 3 rates). Here, we present an alternative method to measure individual transition rates by initializing population in one hyperfine level (or, equivalently, in a single class) within a narrow spectral region and tracking the decay of this state-specific hyperfine population versus its neighboring spectral background. This method can be advantageous for measurements in rare-earth ions with more than one ground hyperfine level, where there are multiple classes of ions since the number of parameters for initial spin population are reduced due to initialization.

We now describe the steps in experiments. We first create a transmission window using spectral tailoring techniques as described in Ref. [47] and initialize the population in one of the ground state hyperfine levels within a spectral region of 1 MHz inside the window. This enables coupling of the laser to a single class of ions and appropriate selection of spectral background range enables us to monitor only this class of ions rather than all the nine classes. The pulse sequence used for creating the transmission window and population initialization are detailed in Appendix A 4. Initial population conditions and evolution for all classes of ions are explained

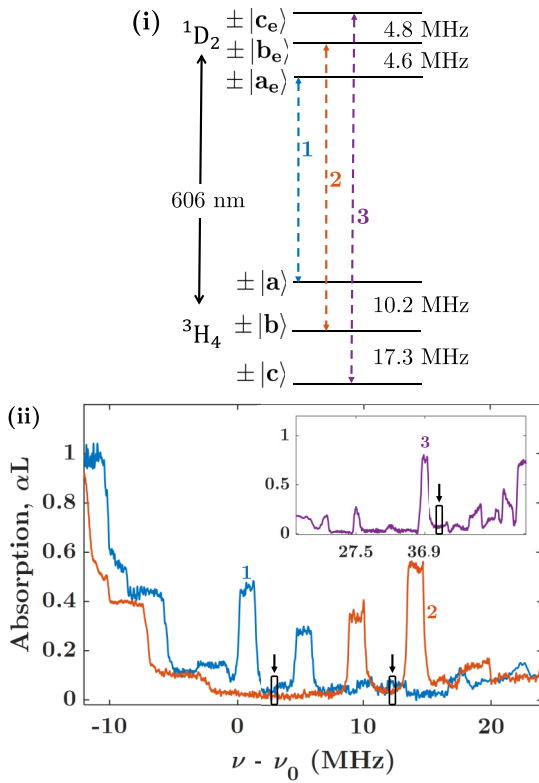


FIG. 2. Hyperfine energy levels in $\text{Pr}^{3+}:\text{Y}_2\text{SiO}_5$ corresponding to the ${}^3H_4 \rightarrow {}^1D_2$ transition at 606 nm and the absorption spectrum obtained from the experiments. (i) Transitions used for evaluating population decay in this experiment are labeled as 1, 2, and 3. (ii) Absorption spectrum after initializing the population in $\pm|a\rangle$ (blue), $\pm|b\rangle$ (red), and $\pm|c\rangle$ (inset, purple). Peaks labeled as 1, 2, and 3 correspond to the transition shown in (i). The background absorption region considered for each of the peaks is marked with black arrows at 2 MHz, 12.2 MHz, and 36.9 MHz.

in Appendix A 3. By probing the ions at different intervals of time, we recorded decay curves for each of the levels, up to 2700 s. The absorption structure was erased and the population was reset using a strong frequency scanning pulse after the last readout. The transmission window was then recreated. Experiments were also carried out in the presence of an external magnetic field in the range 5–10 mT, along the crystal axis b . For each experiment, the field was turned on after the step of population initialization. For a given hyperfine level, the population decays at the same rate (within ± 5 –10%) in the range 5–10 mT. Thus we take the average of the decay for each hyperfine level for this range of magnetic fields.

Transitions used for evaluating the population and an example of the absorption structure after the initialization process within 1 MHz region are shown in Fig. 2. The optical transitions labeled as 1, 2, and 3 in (i) have higher oscillator strength than other transitions; thus the corresponding absorption peaks in (ii) show high absorption and are used for data analysis. Three spectra in blue, red, and purple (inset) show the absorption spectrum after initializing ions in $\pm|a\rangle$, $\pm|b\rangle$, and $\pm|c\rangle$, respectively. Evaluation of population is done in two steps. First, a slope is subtracted across the width of each peak since the background on either side might be different

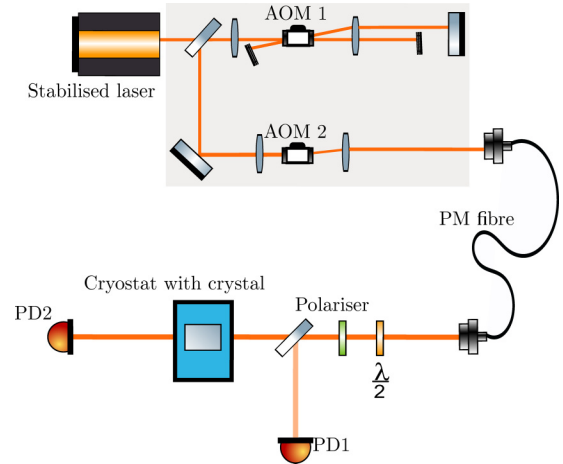


FIG. 3. Stabilized laser light is modulated in frequency and amplitude using “AOM 1” (center frequency 200 MHz) in double pass configuration and “AOM 2” (center frequency 60 MHz). A polarization maintaining fiber guides light onto a different table with the cryostat. Polarization of light is adjusted to be along the D_2 axis using a polarizer and half-wave plate. A portion of incoming light is sent to a reference detector (PD1) and transmission through the crystal is detected by the transmission detector (PD2).

on the low and high frequency sides of the peak. This can be seen, for example, in peak 1 in Fig. 2(ii). Second, the area under the peaks labeled 1 is summed up to obtain the population $\pm|a\rangle$ and the same is done for peaks 2 and 3 to obtain populations in $\pm|b\rangle$ and $\pm|c\rangle$, respectively. Background absorption level is indicated with black arrows at 2 MHz, 12.2 MHz, and 38.9 MHz in Fig. 2. More details can be found in Appendix A 5.

All experiments were done in a $\text{Pr}^{3+}:\text{Y}_2\text{SiO}_5$ crystal with 0.05% concentration and dimensions 10 mm \times 10 mm \times 0.8 mm along D_1 , D_2 , and b axes, respectively. The crystal was placed inside a liquid helium bath cryostat and cooled down to ~ 2 K. The light source was a dye laser tuned to the ${}^3H_4 \rightarrow {}^1D_2$ transition in $\text{Pr}^{3+}:\text{Y}_2\text{SiO}_5$ at 606 nm and was locked to an ultralow expansion glass cavity using the Pound-Drever-Hall locking technique, reducing the linewidth to sub-kHz. A schematic of the experimental setup is shown in Fig. 3. All the pulses were shaped using an arbitrary waveform generator and two AOMs. A half-wave plate in combination with a polarizer aligns the polarization of the light to the D_2 axis of the crystal with an absorption coefficient measured to be 40 cm^{-1} . The optical power of light for burning pulses was about 20 mW. The readout probe had sufficiently low power such that the same absorption structure could be read up to 100 times without disturbing the population. This was checked by reducing the power until the change in absorption after 100 readouts was within shot-to-shot fluctuations. A collimated 1 mm diameter beam, propagating along the b axis (0.8 mm) of the crystal, was used. More details about experiments are described in Appendix A 4.

IV. RESULTS AND DISCUSSION

Results of population decay are shown in Fig. 4. We will first describe the relaxation dynamics in Fig. 4 [(i) and (ii)],

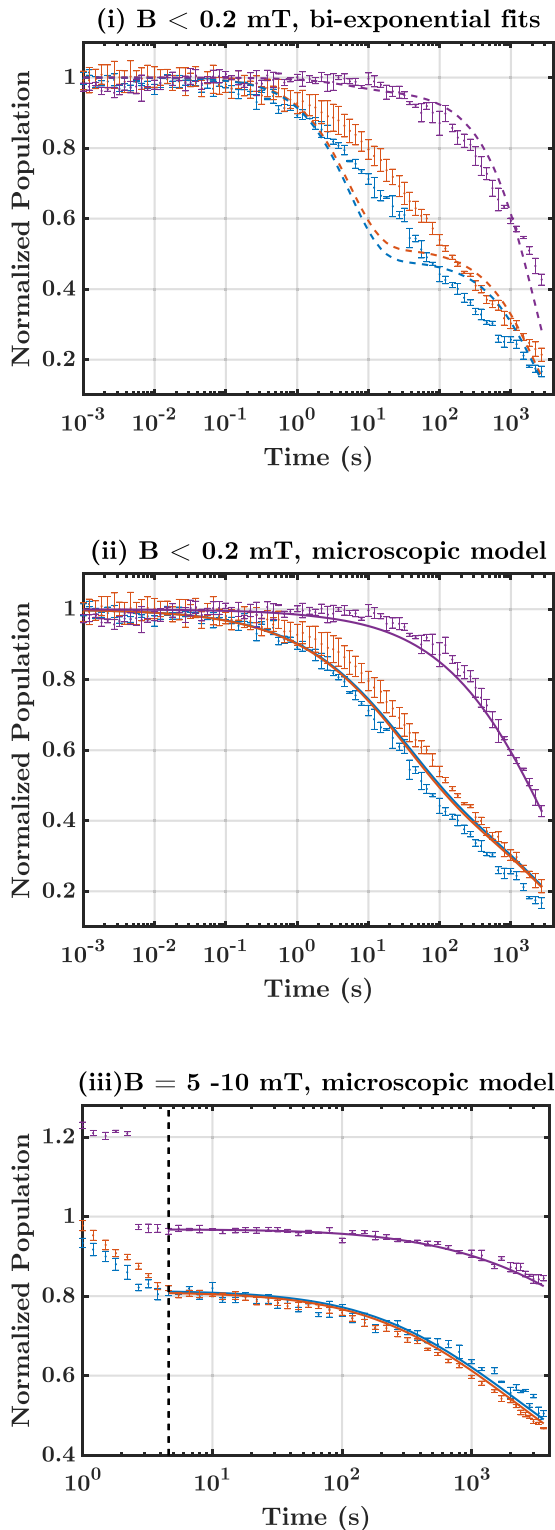


FIG. 4. Population decay of three ground states are shown in three colors: $\pm|a\rangle$ in blue, $\pm|b\rangle$ in red, and $\pm|c\rangle$ in purple. The experimental data is shown with error bars. (i) The colored dashed-dotted lines are the best biexponential fits. (ii) The colored solid lines are the result of simulation using our microscopic model described in Sec. II. (iii) Experimental data and microscopic model simulations with external field of 5–10 mT. The vertical dashed black line shows the time t_0 at which the magnetic field \mathbf{B} is reached after turning it on. See text for details.

in the absence of an applied field. The figures show the experimental data with error bars indicating the weighted standard deviation of three data sets taken for decay after initializing the populations in each hyperfine level $\pm|a\rangle$ (blue), $\pm|b\rangle$ (red), and $\pm|c\rangle$ (purple). There was no external magnetic field applied but previous measurements indicate that there is a residual field <0.2 mT in our cryostat. Population decay for the first 5 ms is negligible so a moving average is performed up to this point and, subsequently, the population is normalized with respect to this point. Decay from $\pm|c\rangle$ is slower than $\pm|a\rangle$ or $\pm|b\rangle$ so one can expect R_{ac} and R_{bc} to be lower than R_{ab} . In other words, ions in $\pm|c\rangle$ flip-flop with those in either of the other levels at a much slower rate. As described earlier in Sec. I, a single average value for each of R_{ab} , R_{bc} , R_{ac} is typically used to describe the relaxation of all ions in the crystal. Thus all ions relax biexponentially with $N = 1$ in Eqs. (A7), (A8), and (A9) in Appendix A3. As an example of this macroscopic model, we attempted a biexponential fit to our data, plotted using dashed-dotted lines in Fig. 4(i). The best fit obtained for $\pm|a\rangle$, $\pm|b\rangle$, and $\pm|c\rangle$, respectively, was $0.52e^{-t/5.52} + 0.48e^{-t/2193}$ (blue), $0.48e^{-t/5.52} + 0.52e^{-t/2193}$ (red), and $0.03e^{-t/5.52} + 0.97e^{-t/2193}$ (purple), where time t is in seconds. While these curves fit well to many data points, several data points do not follow the fits, especially $\pm|a\rangle$ and $\pm|b\rangle$.

Each decay curve obtained in Fig. 4 is, in fact, an average of many exponential decays of different ions within the 1 MHz peak shown in Fig. 2(ii). Each ion may have a different flip-flop rate for a given transition, depending on its position and orientation in the crystal. In the microscopic model, the effective decay is instead an average of the biexponential decay of many ions in the crystal, shown as the solid colored (blue, red, and purple) lines in Fig. 4(ii). These are the simulations which evaluate population according to steps detailed in Sec. II and they match the experimental data quite well. The solid colored lines in Figs. 4(ii) and 4(iii) show the fits from simulation of our microscopic model in the absence and presence of magnetic field, respectively. In addition to the list of steps in simulations described in Sec. II, a few more steps were followed in order to be able to compare the simulations with the experiments.

(1) Using the rates R_{ab} , R_{bc} , and R_{ac} , the population decay in the levels $\pm|a\rangle$, $\pm|b\rangle$, and $\pm|c\rangle$ is calculated using respectively Eqs. (A7), (A8), and (A9) derived in Appendix A3.

(2) Steps (1)–(3) from the list in Sec. II are repeated for $i = 2, 3, \dots, N$, where N is the number of ions in the sphere. An average decay of N ions gives a single decay curve describing the decay of all ions in the crystal. These are the solid colored lines in Fig. 4(iii).

(3) All of the above steps are repeated for data with an external magnetic field.

(4) Parameters Γ_{ab} , Γ_{bc} , Γ_{ac} , κ_{ab} , κ_{bc} , and κ_{ac} are optimized to match the experimental data.

The experiments show little difference between the decay from $\pm|a\rangle$ and $\pm|b\rangle$, indicating that ions occupying these states have the strongest magnetic dipole-dipole interaction. This is shown by the blue and red solid lines almost overlapping with each other in Fig. 4(i). The optimized values of spin inhomogeneous linewidths, Γ_{ab} , Γ_{bc} , and Γ_{ac} , were found to be 0.618, 3.309, and 2.664 kHz, respectively. These values are

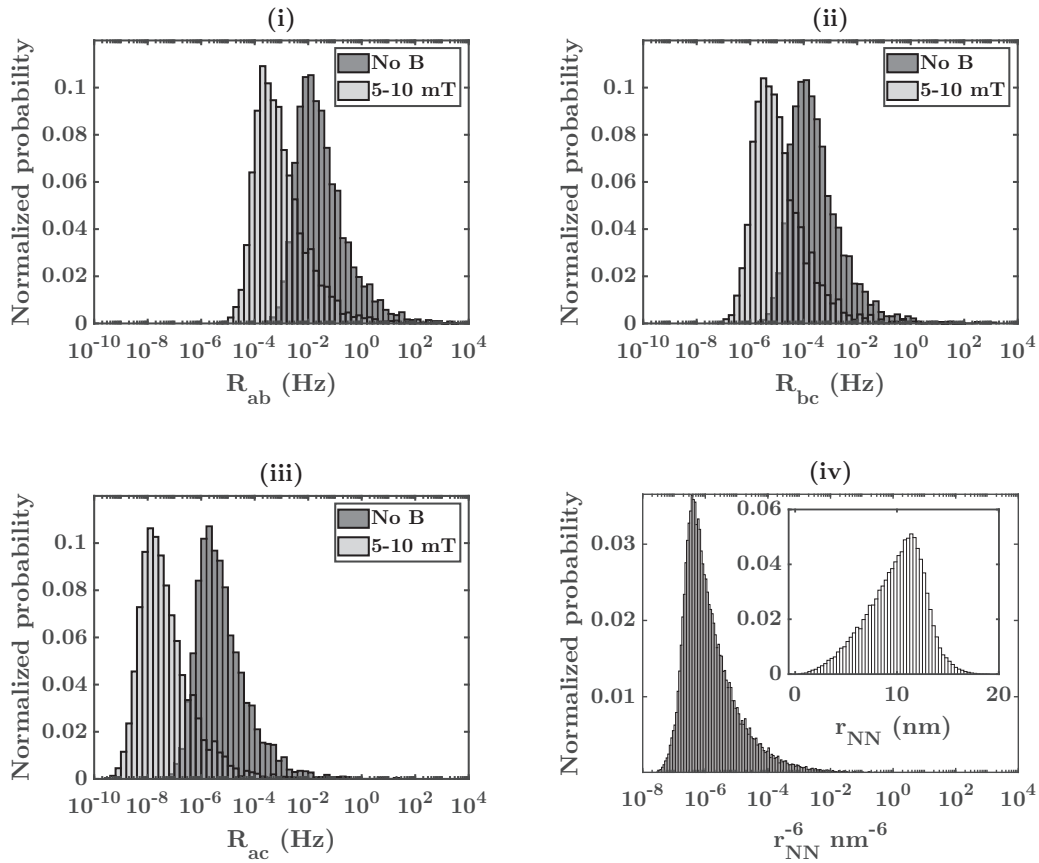


FIG. 5. Effect of magnetic field on the flip-flop rates. Panels (i)–(iii) show a histogram of R_{ab} , R_{bc} , and R_{ac} , respectively, for two cases: residual field < 0.2 mT and external applied field of 5–10 mT. In the presence of residual field, R_{ab} peaks at 10^{-4} Hz, while R_{bc} and R_{ac} peak at 10^{-4} Hz and 2×10^{-6} Hz. All the rates slow down by about two orders of magnitude with a field of 5–10 mT. The distribution of r^{-6} for 20 closest neighboring ions considered in the simulations is shown in (iv). The inset shows the histogram of r , the ion-ion distance.

much lower than previously measured spin inhomogeneities in bulk crystals, e.g., $\Gamma'_{ab} = 50.5$ kHz and $\Gamma'_{bc} = 75.4$ kHz from Ref. [36]. We now try to offer one possible explanation to solve this discrepancy. The measurements in Ref. [36] are sensitive toward the bulk spin inhomogeneity. On the contrary, our simulations show that the main contribution to the flip-flop process occurs between ions that are in the order of 10 nm apart [see inset of Fig. 5(iv)]. Thus we speculate that the local spin inhomogeneity between any two ions situated only 10 nm apart is much less than the measured bulk values, i.e., it lies in the range $\nu_{ab} \pm \Gamma_{ab}$, where Γ_{ab} is in the order of kHz. Finally, this means that on larger scales than 10 nm, the local average of the spin transition frequency, i.e., ν_{ab} , varies in the order of $\Gamma'_{ab} \approx 50$ kHz such that if two ions that are not spatially close are compared, their inhomogeneity is in the order of the observed bulk inhomogeneity. Note, however, that more investigations are needed in order to confirm or deny this hypothesis.

The optimization is fairly insensitive to Γ_{ac} and the relaxation is predominantly governed by the rates R_{ab} and R_{bc} . We now try to understand why the fitted values of the inhomogeneous linewidths, Γ_{ab} and Γ_{bc} differ by a factor of ~ 5.3 . The inhomogeneous linewidths should be proportional to the hyperfine transition energies [48]. Thus, the ratio of the terms Q_{xy} and Q_{yz} in Eq. (4) should be proportional

to the ratio of the inhomogeneous linewidths Γ_{ab} and Γ_{bc} . After the necessary rotations, $Q_{xy} = 0.0982$ MHz and $Q_{yz} = 0.4389$ MHz. The ratio of these values is ~ 4.5 . Another possible contribution to spin inhomogeneity is inhomogeneity in the g tensor, which stems from strains or defects [49]. Local inhomogeneity in spin transition frequencies could also be due to magnetic dipole-dipole interactions between a Pr ion with its neighboring Pr ions of the type given by Eq. (5). If the hyperfine wave functions $\pm|a\rangle$, $\pm|b\rangle$, and $\pm|c\rangle$ were composed of pure $\pm|\frac{1}{2}g\rangle$, $\pm|\frac{3}{2}g\rangle$, and $\pm|\frac{5}{2}g\rangle$ states, then the shift in hyperfine frequencies due to interaction between a pair of Pr ions scales linearly with the quantum number $m_l = \frac{1}{2}, \frac{3}{2}, \frac{5}{2}$. Thus the frequency shift of one ion in a pair occupying $\pm|\frac{3}{2}g\rangle$ and $\pm|\frac{5}{2}g\rangle$ is five times larger than that of another ion in a pair occupying $\pm|\frac{1}{2}g\rangle$ and $\pm|\frac{3}{2}g\rangle$. Furthermore, the effect of external magnetic field is largest on $\pm|c\rangle$ since it undergoes a larger Zeeman shift compared to $\pm|a\rangle$, as seen in Figs. 8(ii) and 8(vi) in Appendix A 5. This could also explain why Γ_{bc} is ~ 5.3 times larger than Γ_{ab} , even though $\pm|a\rangle$, $\pm|b\rangle$, and $\pm|c\rangle$ are actually an admixture of the pure hyperfine states.

For the experiments with magnetic field in Fig. 4(iii), the field is put on after the population initialization step and it takes a few seconds for the field to ramp up to the set value. Thus the simulation evolves the population until the dotted

line at 4.6 s assuming there is no external field and normalizes the data so that the population at the time corresponding to the dotted line in (iii) equals the population in (ii). Some of the data points in $\pm|c\rangle$ in (iii) before the dotted line show population greater than 1. This is an experimental artifact and occurs because the peak corresponding to these points, “3” in Fig. 2, splits in the presence of field due to nuclear Zeeman effect and thus a different spectral region is chosen for evaluating population before and after the peak has split. This is shown in detail in Appendix A 5.

After the dotted line, it is assumed that the magnetic field has reached the set value and the simulation evolves the population by including the phenomenological terms κ_{ab} , κ_{bc} , and κ_{ac} introduced earlier in Eq. (1). The optimized values were found to be respectively 2.6, 3.6, and 1.5 with a field between 5 and 10 mT. Figure 5 shows the effect of magnetic field on the calculated rates, where (i), (ii), and (iii) show the histogram of R_{ab} , R_{bc} , and R_{ac} , respectively, with and without a magnetic field. R_{ab} (with no applied field) is spread over a distribution ranging from 10^{-4} to 10^2 Hz and peaks at 10^{-2} Hz. R_{bc} is slower, ranging from 10^{-6} to 1 Hz and peaks at 10^{-4} Hz, with no field, while R_{ac} is slowest, ranging from 10^{-7} to 1 Hz and peaks at 2×10^{-6} Hz. All three rates slow down by two orders of magnitude with a field of 5–10 mT. The distribution of rates shown in (i)–(iii) follows from the distribution of r_{NN}^{-6} shown in (iv) and the inset shows the distribution of r_{NN} , where r is the distance to any of the 20 closest neighbors of any ion considered in the simulations.

To understand why the rates slow down in a magnetic field, one can infer from Eq. (1) that the cause could either be evolution of matrix elements in the dipole-dipole interaction term or a change in density of states $f(E)$. While the matrix elements do not change appreciably with a small field of 5–10 mT, the density of states changes drastically due to the decrease in homogeneous linewidth by more than a factor of 10, as measured in Ref. [42], and this is attributed to minimizing spin flips of the neighboring Y ions. In the absence of an external field, the magnetic field experienced by the core Y ions is due to the local Pr ion, which is of the order of ~ 0.1 mT, and a change in the spin state of Pr flips the spin state of Y ions. Thus dephasing of Pr ions is dominated by neighboring Y flips in the core. When the external field significantly exceeds the field due to the local Pr ion, such flips are minimized. Another factor contributing to the change in density of states is the increase in the spin inhomogeneous linewidth, characterized by the fitting parameters κ_{ab} , κ_{bc} , and κ_{ac} . A linear increase in spin inhomogeneous linewidths has also been reported in $\text{Nd}^{3+}:\text{Y}_2\text{SiO}_5$ [30] and in erbium doped glass fibers [50]. Measurements of spin linewidths as a function of magnetic field has partly been done in some Kramers ions [51] and similar measurements in $\text{Pr}^{3+}:\text{Y}_2\text{SiO}_5$ may shed more light on this explanation but such data is unavailable at this point.

We conclude this section by noting that there are two conditions that need to be satisfied for two Pr ions to flip-flop: they need to be close to each other in the crystal and they also need to be spectrally close in the spin inhomogeneous profile. In our model, we take an average value for the spin inhomogeneity and model the ion-ion distance as a distribution. One could also model the spin inhomogeneity as a distribution, for example, by including the effect of the local magnetic field

around each Pr ion. The term \mathbf{B} in Eq. (2) could be replaced by $\mathbf{B}_{\text{total}} = \mathbf{B}_{\text{ext}} + \mathbf{B}_{\text{local}}$ so that each ion has a unique spin Hamiltonian, resulting in a distribution of Zeeman frequencies of Pr ion.

V. CONCLUSION

We have presented a method to model microscopic effects of flip-flop interactions between individual ions in a crystal doped by rare-earth ions. We have simulated a random doping based on the crystal structure of the host, where the position and orientation of all ions is known. Every dopant ion is situated in a unique position and orientation with respect to its neighbors so the ion-ion distance is a distribution and the flip-flop rate of any ion with its neighbors is different owing to this distribution. We apply this model to experiments of population decay of ground state hyperfine levels in $\text{Pr}^{3+}:\text{Y}_2\text{SiO}_5$. The experimental method used is an alternative to methods used in earlier works. The collective relaxation dynamics of all ions probed in the crystal is an average sum of many exponential decays of different ions. Thus the flip-flop rate between two hyperfine levels is a distribution of rates rather than one average rate describing the dynamics of all ions.

The fastest rate is R_{ab} between the levels $\pm|a\rangle$ and $\pm|b\rangle$, whose distribution has a peak at 10^{-2} Hz while R_{bc} and R_{ac} have a peak at 10^{-4} and 2×10^{-6} Hz, respectively, in the presence of a residual field < 0.2 mT. All the rates decrease by two orders of magnitude upon applying an external field of 5–10 mT and the reason could be a combination of an order of magnitude decrease in the spin homogeneous linewidths and an increase in spin inhomogeneous linewidths [29,30]. An improvement to the model could be to include the effect of differences in the local magnetic field around each dopant ion. Nonetheless, our model serves as a general tool to calculate other kinds of interactions at the microscopic level. It could be used to study the dynamics of other rare-earth ions in different materials as well.

ACKNOWLEDGMENTS

We thank Prof. P. Samuelsson, Dr. M. Afzelius for useful discussions, and Dr. S. P. Horvath for providing partial code to calculate the spin Hamiltonian. This work was supported by the Knut and Alice Wallenberg Foundation (Grant No. KAW 2016.0081), Wallenberg Center for Quantum Technology (WACQT) funded by the Knut and Alice Wallenberg Foundation (Grant No. KAW 2017.0449), Swedish Research Council (Grants No. 2016-05121 and No. 2019-04949), and European Union FETFLAG program, Grant No. 820391 (SQUARE).

APPENDIX

1. Density of states for transitions between levels in two different continuum of states

In this section, we give details of how Fermi’s rule is applied to the case of a flip-flop transition between two inhomogeneously broadened levels centered around different

energies. We first start with Fermi's rule for a transition between two discrete levels and then extend it to the case of transition between a level in a continuum of states with finite width to another continuum of states. Finally, we apply this to flip-flop transitions, where each state is a two-level system.

Let us start with two levels $|1\rangle$ and $|2\rangle$ with energies E_1 and E_2 , respectively. The transition rate from a discrete state with energy E_1 in $|1\rangle$ to E_2 in $|2\rangle$ under a perturbation H' is given by Fermi's rule:

$$R_{E_1 \rightarrow E_2} = \frac{2\pi}{\hbar} |\langle 1|H'|2\rangle|^2 \delta(E_1 - E_2).$$

Assuming the matrix element $|\langle 1|H'|2\rangle|$ is independent of the energies E_1 and E_2 , the total transition rate from the continuum of states in $|1\rangle \rightarrow |2\rangle$ is given by integrating $R_{E_1 \rightarrow E_2}$ over the density of states for both the initial and final energies, similar to Eq. (6b) in Ref. [52]:

$$\begin{aligned} R_{|1\rangle \rightarrow |2\rangle} &= \int dE_1 dE_2 \rho_1(E_1) \rho_2(E_2) R_{E_1 \rightarrow E_2} \\ &= \frac{2\pi}{\hbar} |\langle 1|H'|2\rangle|^2 \int dE \rho_1(E) \rho_2(E). \end{aligned} \quad (\text{A1})$$

Further, we assume that both ρ_1 and ρ_2 have a normalized Lorentzian line shape centered around ϵ_1 and ϵ_2 with homogeneous HWHM (half width at half maxima) Δ_1 and Δ_2 , respectively, such that $\rho_l(E) = \frac{1}{\pi} \frac{\Delta_l}{\Delta_l^2 + (E - \epsilon_l)^2}$, where $l = 1, 2$. The rate is then

$$R_{|1\rangle \rightarrow |2\rangle} = \frac{2\pi}{\hbar} |\langle 1|H'|2\rangle|^2 \left[\frac{1}{\pi} \frac{\Delta_1 + \Delta_2}{(\Delta_1 + \Delta_2)^2 + (\epsilon_1 - \epsilon_2)^2} \right]. \quad (\text{A2})$$

For the case of flip-flop transitions, the perturbation H' is the magnetic dipole-dipole Hamiltonian between two ions i and j : H_{dd}^{ij} . $|1\rangle$ is the two-level system $|x^i\rangle \otimes |y^j\rangle$, which flips to $|2\rangle$, i.e., $|y^i\rangle \otimes |x^j\rangle$ due to H_{dd}^{ij} , where $|x\rangle, |y\rangle$ are the wave functions of the hyperfine levels $|+a\rangle, |-a\rangle \dots -|c\rangle$ (shown in Fig. 2). In Eq. (A2) above, ϵ_1 and ϵ_2 are the energies of $|x^i\rangle \otimes |y^j\rangle$ and $|y^i\rangle \otimes |x^j\rangle$, respectively, and Δ_1 and Δ_2 are their respective homogeneous HWHM of Lorentzian line shapes. The line shape of such a transition is given by the convolution of the two Lorentzian line shapes of the individual levels and is another Lorentzian with HWHM $\Delta_1 + \Delta_2$, centered at $\epsilon_1 - \epsilon_2$. From Refs. [41,42], we take $2\Delta_1 = \frac{1}{\pi h T_2}$, where T_2 is the spin coherence time at zero magnetic field and it is equal to 0.5 ms (6 ms with a field of 5–10 mT). Considering $\Delta_1 = \Delta_2$, HWHM is $\Delta = \frac{1}{\pi h T_2}$, which is just the homogeneous linewidth of the transition $|x\rangle \leftrightarrow |y\rangle$. Also, $(\epsilon_1 - \epsilon_2) = h\Gamma_{xy}$, where Γ_{xy} is the spin inhomogeneity.

Writing Eq. (A2) in terms of frequencies and replacing $\Delta_1 + \Delta_2$ by $h\Gamma_{\text{hom}}$ and $(\epsilon_1 - \epsilon_2)$ by $h\Gamma_{xy}$, we get the final expression:

$$R_{|x\rangle \rightarrow |y\rangle} = \frac{2\pi}{\hbar} \left| \langle y^j \otimes x^j | H_{dd}^{ij} | x^i \otimes y^j \rangle \right|^2 \left[\frac{1}{\pi h} \frac{\Gamma_{\text{hom}}}{\Gamma_{\text{hom}}^2 + \Gamma_{xy}^2} \right]. \quad (\text{A3})$$

Thus we can use the last term on the right of the above equation as the form of density of states $f(E)$. Similar expressions have been used to describe transitions between broadened

states in different quantum wells, as described in Sec. 3.3 of Ref. [37]. In Eq. (1) in the main text, the homogeneous linewidths are functions of magnetic field and we also have a phenomenological factor κ_{xy} to describe the increase in inhomogeneous linewidths in the presence of magnetic field.

2. Reduction of rates from 15 to 3 and optimization of parameters in simulations

In the absence of an external field, there are three ground state hyperfine levels in $\text{Pr}^{3+}:\text{Y}_2\text{SiO}_5$ and each splits into two in the presence of a field as shown in Fig. 1. There can be fifteen unique rates due to magnetic dipole transitions in this case. Flip-flop interactions where initial and final state are the same or only change parity, for example, $R_{\pm|b\rangle \leftrightarrow \pm|b\rangle}$, are ignored since we do not measure these individually in our experiments. Thus the simulations calculate twelve unique rates. However, our experiments are designed to measure only three rates, $R_{\pm|a\rangle \leftrightarrow \pm|b\rangle}$, $R_{\pm|b\rangle \leftrightarrow \pm|c\rangle}$, and $R_{\pm|a\rangle \leftrightarrow \pm|c\rangle}$, which are referred to in the main article as R_{ab} , R_{bc} , and R_{ac} . Each of the rates is divided by six since the neighboring ion can only be in one of the six hyperfine levels. So we are left with the task of reducing the twelve rates from simulations down to three.

We divide the rates into three categories, each involving the pair of levels $\pm|a\rangle$ and $\pm|b\rangle$, $\pm|b\rangle$ and $\pm|c\rangle$, and $\pm|a\rangle$ and $\pm|c\rangle$. Histogram of rates involving the transitions in each pair are shown in Figs. 6(i), 6(iii), and 6(v). We first consider (i).

(1) Transitions originating from the same level are added together—for example, the rates $|+a\rangle \rightarrow +|b\rangle$ and $|+a\rangle \rightarrow -|b\rangle$ [labeled as (I) and (II) in Fig. 6(i)]. Similarly, (III) and (IV), $-|a\rangle \rightarrow +|b\rangle$ and $-|a\rangle \rightarrow -|b\rangle$ are added together.

(2) Since we cannot distinguish $|+a\rangle \rightarrow +|b\rangle$ from $-|a\rangle \rightarrow +|b\rangle$, we take the average of (I + II) and (III + IV), which is reasonable since they are very similar and, in experiments, the split peaks appear to decay at the same rate [see Figs. 8(iv) and 8(vi) for the case of $\pm|b\rangle$ and $\pm|c\rangle$]. This total rate is called R_{ab} . The relative difference between the two quantities, calculated as $[(\text{I}+\text{II}) - (\text{III}+\text{IV})]/\text{Mean}[R_{ab}]$, is shown in Fig. 6(ii).

A similar argument is applied to (iii),(iv) and (v),(vi) in Fig. 6; thus the rates are reduced from 12 to three.

Optimization of the parameters Γ_{ab} , Γ_{bc} , Γ_{ac} , κ_{ab} , κ_{bc} , and κ_{ac} was done using global search and fminsearch functions in MATLAB. The cost function, which is a measure of deviation in population between simulated model (p_m) and experiments (p_e) is minimized to have the lowest ‘‘score’’ simultaneously for decay in all three hyperfine levels as well as for all values of magnetic field:

$$\text{score} = \sum_{\substack{\forall \text{ times,} \\ \forall \pm|a\rangle, \\ \forall \mathbf{B}}} \left[\frac{p_e - p_m}{w p_e} \right]^2,$$

where we divide by p_e in order to minimize the relative difference instead of the absolute difference. For data without external magnetic field, w is the standard deviation of three data (plotted as the error bars in Fig. 4) sets taken at each time point and for cases with magnetic field and w is the standard deviation of three data sets, each taken at 5, 7, and 10 mT. Normalizing the score with respect to p_e ensures higher weight

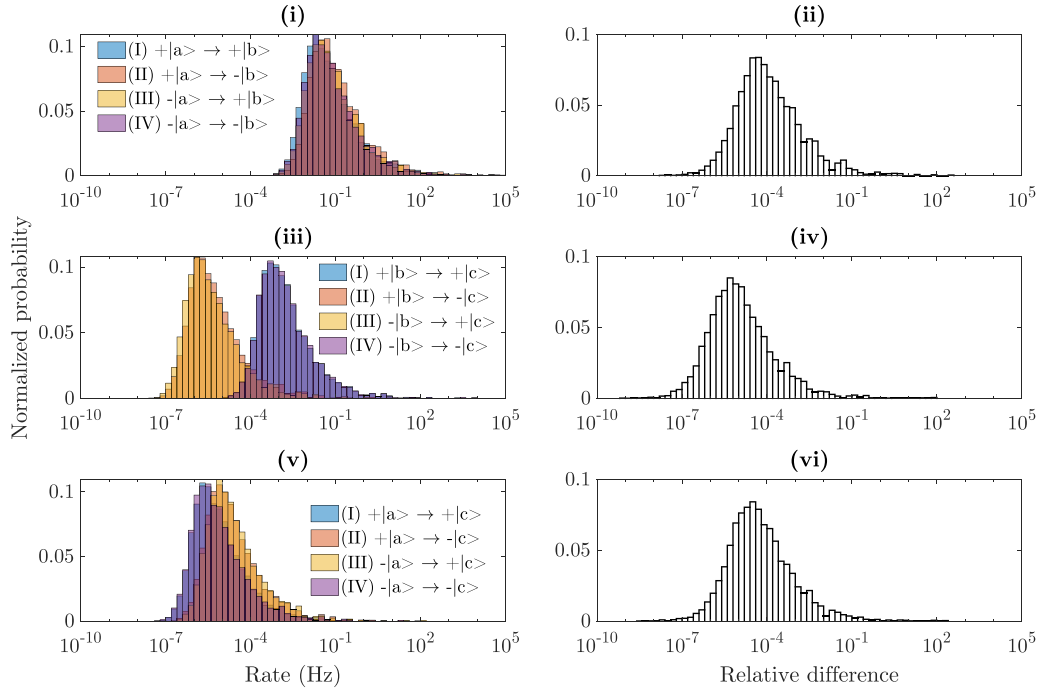


FIG. 6. Histogram of rates of all transitions calculated between each pair of levels without an external magnetic field: (i) $\pm|a\rangle$, $\pm|b\rangle$, (iii) $\pm|b\rangle$, $\pm|c\rangle$, and (v) $\pm|a\rangle$, $\pm|c\rangle$. Relative difference between the quantities (I + II), (III + IV) is shown in panels (ii), (iv), and (vi). Average of (I + II) and (III + IV) is taken to give three effective rates R_{ab} , R_{bc} , and R_{ac} .

is given to population at later times, where the error bars are sometimes quite small. In total, there are six parameters describing the decay: Γ_{ab} , Γ_{bc} , Γ_{ac} , κ_{ab} , κ_{bc} , and κ_{ac} . The score is most sensitive to value of Γ_{ab} . A change of $\pm 5\%$ in Γ_{ab} changes the score by $\sim 10\%$, while the same change in Γ_{bc} or κ_{ab} changes the score by $\sim 3\%$. Changing κ_{bc} by $\pm 5\%$ results in a change in score by $\sim 1.5\%$. Thus the relaxation is mostly governed by the fastest rate, Γ_{ab} . It was also checked that increasing the size of the sphere or number of neighbors did not further improve the score appreciably; thus it is sufficient to calculate the effect of 20 nearest neighbors on each other and in a YSO crystal and this distance varies between 1 and 20 nm.

3. Rate equations and initial conditions of population

In this section, we derive the rate equations for a three level system $\pm|a\rangle$, $\pm|b\rangle$, and $\pm|c\rangle$ shown in Fig. 2 and elucidate the initial conditions of population for nine classes of ions. If N_a , N_b , N_c are populations normalized to the total population N and R_{ab} , R_{bc} , R_{ac} are the flip-flop rates between the three hyperfine levels, the rate equations can be written as

$$\begin{aligned}\frac{dN_a}{dt} &= R_{ab}N_b + R_{ac}N_c - (R_{ab} + R_{ac})N_a, \\ \frac{dN_b}{dt} &= R_{ab}N_a + R_{bc}N_c - (R_{ab} + R_{bc})N_b, \\ \frac{dN_c}{dt} &= R_{ac}N_a + R_{bc}N_b - (R_{ac} + R_{bc})N_c.\end{aligned}$$

The solutions for arbitrary initial conditions $N_a = n_a$, $N_b = n_b$, and $N_c = n_c$ are

$$\begin{aligned}N_a(t) &= \frac{n_a + n_b + n_c}{3} + \frac{1}{6\sigma} \{ e^{-t(K+\sigma)} [n_a A_1 + n_b A_3 \\ &\quad + n_c A_2 + \sigma(2n_a - n_b - n_c)] - e^{-t(K-\sigma)} [n_a A_1 \\ &\quad + n_b A_3 + n_c A_2 - \sigma(2n_a - n_b - n_c)] \}, \quad (\text{A4})\end{aligned}$$

$$\begin{aligned}N_b(t) &= \frac{n_a + n_b + n_c}{3} + \frac{1}{6\sigma} \{ e^{-t(K+\sigma)} [n_a A_3 + n_b A_2 \\ &\quad + n_c A_1 + \sigma(2n_b - n_a - n_c)] - e^{-t(K-\sigma)} [n_a A_3 \\ &\quad + n_b A_2 + n_c A_1 - \sigma(2n_b - n_a - n_c)] \}, \quad (\text{A5})\end{aligned}$$

$$\begin{aligned}N_c(t) &= \frac{n_a + n_b + n_c}{3} + \frac{1}{6\sigma} \{ e^{-t(K+\sigma)} [n_a A_2 + n_b A_1 \\ &\quad + n_c A_3 + \sigma(2n_c - n_b - n_a)] - e^{-t(K-\sigma)} [n_a A_2 \\ &\quad + n_b A_1 + n_c A_3 - \sigma(2n_c - n_b - n_a)] \}, \quad (\text{A6})\end{aligned}$$

where

$$\begin{aligned}A_1 &= R_{ab} + R_{ac} - 2R_{bc}, \\ A_2 &= R_{ab} + R_{bc} - 2R_{ac}, \\ A_3 &= R_{ac} + R_{bc} - 2R_{ab}, \\ K &= R_{ab} + R_{ac} + R_{bc}, \\ \sigma &= \{ R_{ab}^2 + R_{ac}^2 + R_{bc}^2 - R_{ab}R_{ac} - R_{ab}R_{bc} - R_{ac}R_{bc} \}^{1/2}.\end{aligned}$$

Due to the optical inhomogeneous broadening, the laser can couple to nine different transitions from the ground to excited state (shown in Fig. 2) at a given frequency. To extract the individual rates R_{ab} , R_{bc} , and R_{ac} from a simple hole burning spectra, one would need to follow the evolution of

TABLE I. Conditions of population after initializing ions in $\pm|a\rangle$ state at 0 MHz.

Class	Transition probed at 0 MHz	$f_{\text{peak}} = 0 \text{ MHz}$			$f_{\text{background}} = 2 \text{ MHz}$		
		n_a	n_b	n_c	n_a	n_b	n_c
I	$\pm a\rangle \rightarrow \pm a_e\rangle$	1	0	0	0	0	1
II	$\pm a\rangle \rightarrow \pm b_e\rangle$	0	0	1	0	0	1
III	$\pm a\rangle \rightarrow \pm c_e\rangle$	0	0	1	0	0	1
IV	$\pm b\rangle \rightarrow \pm a_e\rangle$	0	0	1	0	0	1
V	$\pm b\rangle \rightarrow \pm b_e\rangle$	1	0	0	1	0	0
VI	$\pm b\rangle \rightarrow \pm c_e\rangle$	1	0	0	1	0	0
VII	$\pm c\rangle \rightarrow \pm a_e\rangle$	1	0	0	1	0	0
VIII	$\pm c\rangle \rightarrow \pm b_e\rangle$	1	0	0	1	0	0
IX	$\pm c\rangle \rightarrow \pm c_e\rangle$	1	0	0	1	0	0

all classes [35] by summing over contributions from nine transitions for each of the three levels with three unknown initial conditions, thereby giving 30 unknowns. We simplify this by creating a transmission window using optical pumping and isolating peaks of ions in one hyperfine level within this window. A simulation in a six level system (with three ground states and three excited states) was performed to predict an absorption spectra after the initialization step.

An example of initializing in $\pm|a\rangle$, with a peak at 0 MHz corresponding to $\pm|a\rangle \rightarrow \pm|a_e\rangle$, is shown in Fig. 7. It can be seen that the experimental data in purple matches quite well with the black line showing the simulation, indicating successful isolation of one class of ions from the other eight classes. We call this isolated group of ions class I, for which the starting conditions after the initialization are $n_a = 1$, $n_b = 0$, and $n_c = 0$. The corresponding spectral background region at 2 MHz has all class I ions shelved in n_c . The initial population conditions of the other eight classes for both the peak and background are charted out in Table I. The conditions for all classes but one, “I,” are the same for both peak and background. Thus we can subtract background from the peak for this class only using Eq. (A4) to calculate population decay in $\pm|a\rangle$. This describes the decay of an ion i . To account for all ions $i = 1, 2, \dots, N$ in the sphere considered in the simulations, we take the average as follows:

$$N_a(t)|_{\text{class I}} = \frac{1}{N} \sum_i^N (N_{a,\text{peak}} - N_{a,\text{background}})$$

$$= \frac{1}{N} \sum_i^N \frac{1}{2\sigma^i} [(\sigma^i + R_{ac}^i - R_{bc}^i)e^{-t(K^i + \sigma^i)} + (\sigma^i - R_{ac}^i + R_{bc}^i)e^{-t(K^i - \sigma^i)}]. \quad (\text{A7})$$

Similar considerations for peaks corresponding to $\pm|b\rangle \rightarrow \pm|b_e\rangle$ at 14.8 MHz and $\pm|c\rangle \rightarrow \pm|c_e\rangle$ at 36.9 MHz (peaks “2” and “3,” respectively, in Fig. 2) are given in Tables II and III. Coupled with simulations similar to Fig. 7, isolation of one class was ensured. The evolution of population $N_b(t)$ and $N_c(t)$ can also be obtained:

$$N_b(t)|_{\text{class V}} = \frac{1}{N} \sum_i^N (N_{b,\text{peak}} - N_{b,\text{background}}) = \frac{1}{N} \sum_i^N \frac{1}{2\sigma^i} [(\sigma^i - R_{ac}^i + R_{bc}^i)e^{-t(K^i + \sigma^i)} + (\sigma^i + R_{ac}^i - R_{bc}^i)e^{-t(K^i - \sigma^i)}], \quad (\text{A8})$$

$$N_c(t)|_{\text{class IX}} = \frac{1}{N} \sum_i^N (N_{c,\text{peak}} - N_{c,\text{background}}) = \frac{1}{N} \sum_i^N \frac{1}{2\sigma^i} [(\sigma^i + R_{ac}^i - R_{ab}^i)e^{-t(K^i + \sigma^i)} + (\sigma^i + R_{ab}^i - R_{ac}^i)e^{-t(K^i - \sigma^i)}]. \quad (\text{A9})$$

TABLE II. Conditions of population for initializing ions in $\pm|b\rangle$ state at 14.7 MHz.

Class	Transition probed at 14.7 MHz	$f_{\text{peak}} = 14.7 \text{ MHz}$			$f_{\text{background}} = 12.2 \text{ MHz}$		
		n_a	n_b	n_c	n_a	n_b	n_c
I	$\pm a\rangle \rightarrow \pm a_e\rangle$	0	0	1	0	0	1
II	$\pm a\rangle \rightarrow \pm b_e\rangle$	0	0	1	0	0	1
III	$\pm a\rangle \rightarrow \pm c_e\rangle$	0	0	1	0	0	1
IV	$\pm b\rangle \rightarrow \pm a_e\rangle$	0	0	1	0	0	1
V	$\pm b\rangle \rightarrow \pm b_e\rangle$	0	1	0	0	0	1
VI	$\pm b\rangle \rightarrow \pm c_e\rangle$	0	0	1	0	0	1
VII	$\pm c\rangle \rightarrow \pm a_e\rangle$	1	0	0	1	0	0
VIII	$\pm c\rangle \rightarrow \pm b_e\rangle$	1	0	0	1	0	0
IX	$\pm c\rangle \rightarrow \pm c_e\rangle$	1	0	0	1	0	0

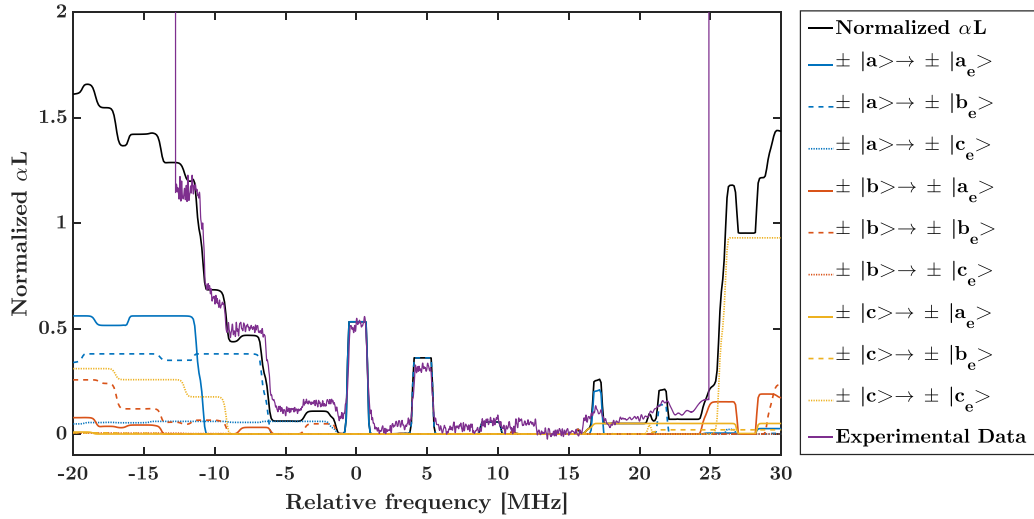


FIG. 7. Simulation of absorption spectrum after initializing population in $\pm|a\rangle$. The black line shows the total absorption, while colored lines show the absorption corresponding to a particular transition, indicated in the legend. Note the three peaks at 0, 4.6, and 9.4 MHz, which have ions absorbing only from $\pm|a\rangle$, indicating successful isolation of one class from the other eight classes. Purple line corresponds to the first readout at 1 ms after the initialization step in the experiments.

4. Experimental details

The light source is a Coherent 699-21 dye laser, optically pumped at 532 nm by a Verdi-V6 solid state laser. The dye solution was made using Rhodamine 6G mixed with ethylene glycol and pumped at 4.2 bar and cooled to 10 °C. All the pulses were shaped using an arbitrary waveform generator (Tektronix AWG520) and two AOMs: “AOM 1” AA.ST.200/B100/A0.5-vis in double pass (in the same configuration as described in [53]) and “AOM 2” A.ST.360/B200/A0.5-vis in single pass. Diffracted light from AOM 2 is coupled to a polarization-maintaining fiber to another table with the cryostat. A beam sampler (90 : 10) is used to reflect some light onto a reference detector PD1 while transmitting the majority of the light towards the crystal. Both detectors used were Thorlabs PDB150A. The absorption as a function of frequency is obtained by scanning over the desired frequency range with a rate of 1 MHz/ μ s with a weak probe. Due to the fast readout scan rate, the transmission signal contains free induction decay from each peak that needs to be deconvoluted as described in [54].

The basic principle involved in creating the transmission window is optical pumping and the reader is referred to Refs. [47,55] for a thorough explanation. The type of pulses used are “sechscan” pulses, listed in Table IV. These are similar to the complex secant hyperbolic pulse but the frequency scanning is done at a constant amplitude and the edges of this scan are rounded in the shape of a sechyp. For more details on this kind of pulse, the reader is referred to Refs. [53,56]. For definitions of the above parameters, the reader is referred to Appendix B in Ref. [57]. The pulse parameters used here are $f_{\text{width}} = 500$ kHz, $t_{\text{FWHM}} = 3$ μ s, and $t_g = 86$ μ s. The frequency scan range is f_{scan} , set by the start and end frequencies ν_{start} and ν_{end} , respectively. The Rabi frequency of each pulse is adjusted to target the transitions listed in column “Transition.” These pulses (“BurnPit”) are repeated in the following sequence.

- (1) Repeat 120 times: BurnPit4 and BurnPit5.
- (2) Repeat 90 times: BurnPit1–3 and BurnPit5–8.
- (3) Repeat 40 times: BurnPit1–3 and BurnPit5.
- (4) Repeat 60 times: BurnPit4 and BurnPit6–8.
- (5) Repeat 60 times: BurnPit7.

TABLE III. Conditions of population for initializing ions in $\pm|c\rangle$ state at 36.9 MHz.

Class	Transition	$f_{\text{peak}} = 36.9$ MHz			$f_{\text{background}} = 38.9$ MHz		
		n_a	n_b	n_c	n_a	n_b	n_c
I	$\pm a\rangle \rightarrow \pm a_e\rangle$	0	0	1	0	0	1
II	$\pm a\rangle \rightarrow \pm b_e\rangle$	0	0	1	0	0	1
III	$\pm a\rangle \rightarrow \pm c_e\rangle$	0	0	1	0	0	1
IV	$\pm b\rangle \rightarrow \pm a_e\rangle$	0	0	1	0	0	1
V	$\pm b\rangle \rightarrow \pm b_e\rangle$	0	0	1	0	0	1
VI	$\pm b\rangle \rightarrow \pm c_e\rangle$	0	0	1	0	0	1
VII	$\pm c\rangle \rightarrow \pm a_e\rangle$	1	0	0	1	0	0
VIII	$\pm c\rangle \rightarrow \pm b_e\rangle$	1	0	0	1	0	0
IX	$\pm c\rangle \rightarrow \pm c_e\rangle$	0	0	1	1	0	0

TABLE IV. Sequence of pulses used for creating the transmission window, with the start and end frequencies of f_{scan} . The Rabi frequency used for each pulse is adjusted to target the transitions listed in the column Transition.

Pulse	ν_{start} (MHz)	ν_{end} (MHz)	Transition
BurnPit1	+32	+24	$\pm b\rangle \rightarrow \pm a_e\rangle$
BurnPit2	+24	+16	$\pm b\rangle \rightarrow \pm c_e\rangle$
BurnPit3	+16.1	+7.5	$\pm b\rangle \rightarrow \pm c_e\rangle$
BurnPit4	-17	-9	$\pm c\rangle \rightarrow \pm c_e\rangle$
BurnPit5	-9	-1	$\pm c\rangle \rightarrow \pm a_e\rangle$
BurnPit6	+7.5	-1.1	$\pm b\rangle \rightarrow \pm a_e\rangle$
BurnPit7	-1.1	+7.5	$\pm c\rangle \rightarrow \pm a_e\rangle$
BurnPit8	+7.5	+15.95	$\pm c\rangle \rightarrow \pm a_e\rangle$

Each pulse is followed by a waiting pulse of 1 ms to allow the system to decay to the ground states. This step empties the $\pm|a\rangle$ and $\pm|b\rangle$ levels and shelves the ions to $\pm|c\rangle$. For population initialization in either $\pm|a\rangle$ or $\pm|b\rangle$, a weak sechscan pulse (“BurnBack”) targeting the transition $\pm|c\rangle \rightarrow |a_e\rangle$ was used repeatedly. This sequence “burns back” ions to $\pm|a\rangle$ and $\pm|b\rangle$. Depending on the target initialization state, ions in $\pm|a\rangle$ or $\pm|b\rangle$ are cleaned away.

To initialize ions in $\pm|c\rangle$, the transmission window is created by shifting all the “BurnPit” pulses by $f_0 = -27.5$ MHz to target another class of ions and empty the $\pm|c\rangle$ level. Then, ions are initialized in $\pm|c\rangle$ by burning back from the transition $\pm|a\rangle \rightarrow |c_e\rangle$ at $f_0 + 4.8 + 4.6$ MHz. Any ions absorbing inside the transmission window that belong to a different ion class than intended are cleaned away using sechscan pulses with the same parameters as the BurnPit pulses. The pulse parameters for the burn back pulses used here are $f_{\text{width}} = 120$ kHz, $t_{\text{FWHM}} = 11.6$ μs , $t_g = 150$ μs , and $f_{\text{scan}} = 1$ MHz.

5. Absorption spectra with and without magnetic field

Absorption spectra from the first and last readout are shown in Fig. 8. Panels (i), (iii), and (v) show the absorption after initializing the populations in $\pm|a\rangle$ (blue), $\pm|b\rangle$ (orange), and $\pm|c\rangle$ (purple), respectively. All black traces show the absorption after the last readout at $t_f = 2700$ s. Although no external magnetic field was applied in these cases, we expect there to be a stray field less than 0.2 mT. Results of similar

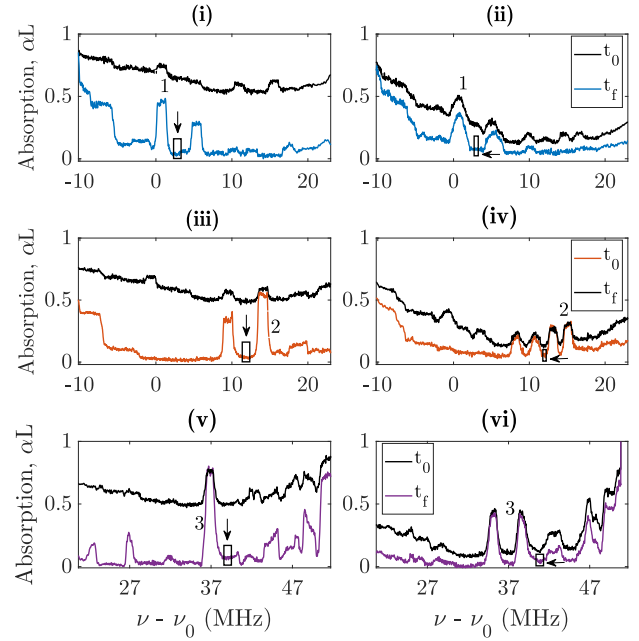


FIG. 8. Absorption structure after the first and last readout at times t_0 and t_f , respectively. (i), (iii), (v) Population initialized at t_0 in one of the three ground states shown in three colors: $\pm|a\rangle$ in blue, $\pm|b\rangle$ in red, and $\pm|c\rangle$ in purple. Peaks used for evaluating population and corresponding background region are indicated similar to Fig. 2. The black traces show the same absorption after the last readout at t_f . The absorption increases over time as the ions which were optically pumped to other frequencies during initialization start to flip-flop into the transmission window. Panels (ii), (iv), and (vi) show the same experiments as (i), (iii), and (v) but with an external field of 10 mT.

experiments with an external field of 10 mT are shown in panels (ii), (iv), and (vi). The first readout t_0 is at 3.8 s for (ii) and (iv), and 5.5 s for (vi), which is also indicated by the vertical dashed line in Fig. 4. Peaks “2” and “3” in (iv) and (vi), respectively, split due to the nuclear Zeeman effect. Although the absorption level of split peaks is roughly halved, the absorption level of their backgrounds is not the same as their counterparts in (iii) and (v). Due to this, some of the data points before the dotted line in Fig. 4(iii) are greater than 1. A different choice of background could perhaps have been better but the important information for simulations is what happens to the population after the magnetic field has reached the set value at the dotted line.

[1] F. Könz, Y. Sun, C. W. Thiel, R. L. Cone, R. W. Equall, R. L. Hutcheson, and R. M. Macfarlane, *Phys. Rev. B* **68**, 085109 (2003).
 [2] R. Oswald, M. G. Hansen, E. Wiens, A. Y. Nevsky, and S. Schiller, *Phys. Rev. A* **98**, 062516 (2018).
 [3] M. Zhong, M. P. Hedges, R. L. Ahlefeldt, J. G. Bartholomew, S. E. Beavan, S. M. Wittig, J. J. Longdell, and M. J. Sellars, *Nature (London)* **517**, 177 (2015).
 [4] M. Nilsson and S. Kröll, *Opt. Commun.* **247**, 393 (2005).

[5] M. Nicolle, J. N. Becker, C. Weinzetl, I. A. Walmsley, and P. M. Ledingham, *Opt. Lett.* **46**, 2948 (2021).
 [6] M. Afzelius and C. Simon, *Phys. Rev. A* **82**, 022310 (2010).
 [7] N. Ohlsson, R. Krishna Mohan, and S. Kröll, *Opt. Commun.* **201**, 71 (2002).
 [8] R. L. Ahlefeldt, M. J. Pearce, M. R. Hush, and M. J. Sellars, *Phys. Rev. A* **101**, 012309 (2020).
 [9] M. Grimm, A. Beckert, G. Aepli, and M. Müller, *PRX Quantum* **2**, 010312 (2021).

- [10] A. Kinos, L. Rippe, D. Serrano, A. Walther, and S. Kröll, *Phys. Rev. A* **105**, 032603 (2022).
- [11] A. Kinos, D. Hunger, R. Kolesov, K. Mølmer, H. de Riedmatten, P. Goldner, A. Tallaire, L. Morvan, P. Berger, S. Welinski, K. Karrai, L. Rippe, S. Kröll, and A. Walther, [arXiv:2103.15743](https://arxiv.org/abs/2103.15743).
- [12] P. B. Sellin, N. M. Strickland, J. L. Carlsten, and R. L. Cone, *Opt. Lett.* **24**, 1038 (1999).
- [13] T. Böttger, G. J. Pryde, and R. L. Cone, *Opt. Lett.* **28**, 200 (2003).
- [14] M. J. Thorpe, L. Rippe, T. M. Fortier, M. S. Kirchner, and T. Rosenband, *Nat. Photon.* **5**, 688 (2011).
- [15] S. P. Horvath, C. Shi, D. Gustavsson, A. Walther, A. Kinos, S. Kröll, and L. Rippe, *New J. Phys.* **24**, 033034 (2022).
- [16] Y. Li, H. Zhang, C. Kim, K. H. Wagner, P. Hemmer, and L. V. Wang, *Appl. Phys. Lett.* **93**, 011111 (2008).
- [17] H. Zhang, M. Sabooni, L. Rippe, C. Kim, S. Kröll, L. V. Wang, and P. R. Hemmer, *Appl. Phys. Lett.* **100**, 131102 (2012).
- [18] X. Xu, S.-R. Kothapalli, H. Liu, and L. V. Wang, *J. Biomed. Opt.* **15**, 066018 (2010).
- [19] C. Venet, M. Bocoum, J.-B. Laudereau, T. Chaneliere, F. Ramaz, and A. Louchet-Chauvet, *Opt. Lett.* **43**, 3993 (2018).
- [20] D. Hill, A. Bengtsson, T. Erlöv, M. Cinthio, and S. Kröll, *Biomed. Opt. Express* **12**, 3196 (2021).
- [21] Q. Li, Ph.D. thesis, Lund University, 2018.
- [22] A. Bengtsson, Ph.D. thesis, Lund University, 2022.
- [23] Y. Yan, C. Y. Shi, A. Kinos, H. Syed, S. P. Horvath, A. Walther, L. Rippe, X. Chen, and S. Kröll, *npj Quantum Inf.* **7**, 138 (2021).
- [24] G. H. Larson and C. D. Jeffries, *Phys. Rev.* **141**, 461 (1966).
- [25] A. Abragam and B. Bleaney, *Electron Paramagnetic Resonance of Transition Ions* (Oxford University Press, Oxford, 2012).
- [26] R. Orbach and B. Bleaney, *Proc. R. Soc. London A* **264**, 458 (1961).
- [27] G. K. Liu, J. Huang, R. L. Cone, and B. Jacquier, *Phys. Rev. B* **38**, 11061 (1988).
- [28] N. Ohlsson, M. Nilsson, and S. Kröll, *Phys. Rev. A* **68**, 063812 (2003).
- [29] B. Car, L. Veissier, A. Louchet-Chauvet, J.-L. Le Gouët, and T. Chanelière, *Phys. Rev. B* **100**, 165107 (2019).
- [30] E. Z. Cruzeiro, A. Tiranov, I. Usmani, C. Laplane, J. Lavoie, A. Ferrier, P. Goldner, N. Gisin, and M. Afzelius, *Phys. Rev. B* **95**, 205119 (2017).
- [31] Y. J. Uemura, T. Yamazaki, D. R. Harshman, M. Senba, and E. J. Ansaldo, *Phys. Rev. B* **31**, 546 (1985).
- [32] K. Holliday, M. Croci, E. Vauthey, and U. P. Wild, *Phys. Rev. B* **47**, 14741 (1993).
- [33] R. C. Johnson, B. Z. Malkin, J. S. Lord, S. R. Giblin, A. Amato, C. Baines, A. Lascialfari, B. Barbara, and M. J. Graf, *Phys. Rev. B* **86**, 014427 (2012).
- [34] E. S. Petersen, A. M. Tyryshkin, J. J. L. Morton, E. Abe, S. Tojo, K. M. Itoh, M. L. W. Thewalt, and S. A. Lyon, *Phys. Rev. B* **93**, 161202(R) (2016).
- [35] R. Klieber, A. Michalowski, R. Neuhaus, and D. Suter, *Phys. Rev. B* **68**, 054426 (2003).
- [36] M. Lovrić, P. Glasenapp, and D. Suter, *Phys. Rev. B* **85**, 014429 (2012).
- [37] A. Wacker, *Phys. Rep.* **357**, 1 (2002).
- [38] P. Villars and K. Cenzual (eds.), Y_2SiO_5 ($Y_2[SiO_4]O$ ht) crystal structure: Datasheet from Pauling File Multinaries Edition–2012 in *SpringerMaterials* Springer-Verlag, Berlin, Heidelberg, Material Phases Data System (MPDS), Switzerland & National Institute for Materials Science (NIMS), Japan, 2016.
- [39] L. Gomes, L. C. Courrol, L. V. G. Tarelho, and I. M. Ranieri, *Phys. Rev. B* **54**, 3825 (1996).
- [40] A. Kinos, L. Rippe, A. Walther, and S. Kröll, *Phys. Rev. A* **105**, 032608 (2022).
- [41] E. Fraval, M. J. Sellars, and J. J. Longdell, *Phys. Rev. Lett.* **92**, 077601 (2004).
- [42] E. Fraval, M. Sellars, A. Morrison, and A. Ferris, Proceedings of the 8th International Meeting on Hole Burning, Single Molecule, and Related Spectroscopies: Science and Applications, *J. Lumin.* **107**, 347 (2004).
- [43] B. S. Ham, M. S. Shahriar, M. K. Kim, and P. R. Hemmer, *Opt. Lett.* **22**, 1849 (1997).
- [44] R. M. Shelby, R. M. Macfarlane, and C. S. Yannoni, *Phys. Rev. B* **21**, 5004 (1980).
- [45] T. L. Bohan and H. J. Stapleton, *Phys. Rev.* **182**, 385 (1969).
- [46] T. Blasberg and D. Suter, *Chem. Phys. Lett.* **215**, 668 (1993).
- [47] M. Nilsson, L. Rippe, S. Kröll, R. Klieber, and D. Suter, *Phys. Rev. B* **70**, 214116 (2004).
- [48] M. Lovrić, P. Glasenapp, D. Suter, B. Tumino, A. Ferrier, P. Goldner, M. Sabooni, L. Rippe, and S. Kröll, *Phys. Rev. B* **84**, 104417 (2011).
- [49] A. M. Stoneham, *Rev. Mod. Phys.* **41**, 82 (1969).
- [50] E. Saglamyurek, T. Lutz, L. Veissier, M. P. Hedges, C. W. Thiel, R. L. Cone, and W. Tittel, *Phys. Rev. B* **92**, 241111(R) (2015).
- [51] S. Welinski, C. Thiel, J. Dajczgewand, A. Ferrier, R. Cone, R. Macfarlane, T. Chanelière, A. Louchet-Chauvet, and P. Goldner, *Opt. Mater. (Amsterdam)* **63**, 69 (2017).
- [52] N. Bloembergen, S. Shapiro, P. S. Pershan, and J. O. Artman, *Phys. Rev.* **114**, 445 (1959).
- [53] L. Rippe, M. Nilsson, S. Kröll, R. Klieber, and D. Suter, *Phys. Rev. A* **71**, 062328 (2005).
- [54] T. Chang, M. Tian, R. K. Mohan, C. Renner, K. D. Merkel, and W. R. Babbitt, *Opt. Lett.* **30**, 1129 (2005).
- [55] A. Walther, Coherent processes in rare-earth-ion-doped solids, Atomic Physics, Department of Physics, Lund University (Lund University, 2008).
- [56] M. Tian, T. Chang, K. D. Merkel, and W. Randall, *Appl. Opt.* **50**, 6548 (2011).
- [57] A. Kinos, L. Rippe, S. Kröll, and A. Walther, *Phys. Rev. A* **104**, 052624 (2021).